A&A, 710, A65 (2026)
https://doi.org/10.1051/0004-6361/202558229

Astronomy & Astrophysics

Metal enrichment of galaxies in a massive node of the cosmic web at $z \sim 3$

X. Wang[1,2,⋆], S. Cantalupo[2], W. Wang[2], M. Galbiati[2], C. C. Steidel[4], A. Pensabene[2], S. Mao[3], A. Travascio[2], T. Lazeyras[2], N. Ledos[2], and G. Quadri[2]

[1] Department of Astronomy, Tsinghua University, Beijing 100084, China
[2] Dipartimento di Fisica, Università degli Studi di Milano-Bicocca, Piazza della Scienza 3, 20126 Milano, Italy
[3] Department of Astronomy, Westlake University, Hangzhou 310030, Zhejiang Province, China
[4] Cahill Center for Astronomy and Astrophysics, California Institute of Technology, MS 249-17, Pasadena, CA 91125, USA

Received 24 November 2025 / Accepted 30 March 2026

ABSTRACT

We present the mass-metallicity relation for star-forming galaxies in the protocluster MUSE Quasar Nebula 01 (MQN01) field, a massive cosmic-web node at $z \sim 3.245$, hosting one of the highest overdensities of galaxies and active galactic nuclei found so far at $z > 3$. Through *James Webb* Space Telescope (JWST) Near Infrared Spectrograph (NIRSpec) spectra and images from JWST and *Hubble* Space Telescope (HST), we identified a sample of nine star-forming galaxies in the MQN01 field with a detection of nebular emission lines (Hβ, [OIII], Hα, [NII]), covering the mass range of $10^{7.5}\,M_\odot$–$10^{10.5}\,M_\odot$. We present the relations of the emission line flux ratios versus stellar mass for the sample and derive the gas-phase metallicity ($12+\log(\mathrm{O/H})$) based on the strong-line diagnostics of [OIII]λ5008/Hβ and [NII]λ6585/Hα. Compared to the typical field galaxies at similar redshifts, MQN01 galaxies show relatively higher [NII]λ6585/Hα and lower [OIII]λ5008/Hβ at the same stellar mass, which implies a higher metallicity by about 0.26 ± 0.07 dex than on the field mass-metallicity relation. These differences decrease when we consider the fundamental metallicity relation, that is, when we also take the galaxy star formation rates into account. We argue that these results are consistent with a scenario in which galaxies in overdense regions assemble their stellar mass more efficiently (or, equivalently, start forming mass at earlier epochs) than field galaxies at similar redshifts.

Key words. galaxies: evolution – galaxies: fundamental parameters – galaxies: high-redshift – galaxies: ISM – galaxies: star formation – large-scale structure of Universe

1. Introduction

Galaxies evolve within ecosystems, exchanging material with the environments through processes including gas accretion, mergers, galaxy interactions, and feedback from stars and active galactic nuclei (AGNs). These processes vary across environments and play critical roles in shaping the galaxy properties (Dekel et al. 2009; Somerville & Davé 2015; Tumlinson et al. 2017). At $z < 1$, observations have shown that galaxies located in dense environments such as clusters tend to be more massive and have lower star formation rates (SFRs; e.g., Baldry et al. 2006; Peng et al. 2010; van der Burg et al. 2020; McNab et al. 2021). The relative importance of different physical mechanisms in shaping galaxy properties is still unclear. At higher redshifts, the cosmic environment is different from the local universe, with a much higher molecular and neutral gas density, a more intense star formation activity, and potentially stronger feedback (e.g., Shapley et al. 2003; Steidel et al. 2010; Tacconi et al. 2010; Behroozi et al. 2013; Lilly et al. 2013; Madau & Dickinson 2014; Popping et al. 2014; Speagle et al. 2014; Genzel et al. 2015). To understand the properties of today's most massive galaxies, it is crucial to study their progenitors under these distinct environmental conditions. The progenitors of present-day massive galaxies living in clusters are found in environments called protoclusters, which are natural laboratories for us to investigate the environmental effects. Observations of protoclusters have shown that galaxies tend to have higher SFRs with larger fractions of massive galaxies and AGNs, consistent with stronger interactions and gas accretion that may contribute to more intense star formation activities (e.g., Steidel et al. 2005; Koyama et al. 2013a,b).

Metallicity is a key property for understanding galaxy star formation histories. Throughout this paper, we use the word metal or metallicity to refer to the gas-phase oxygen abundance, 12 + log(O/H). The metal enrichment and dilution are highly affected by galaxy star formation, feedback, gas inflows, and galaxy interactions. Metallicity has been found to be tightly related to the galaxy stellar mass in a wide mass range, and this relation is known as the mass-metallicity relation (e.g., Tremonti et al. 2004; Erb et al. 2006; Maiolino et al. 2008; Steidel et al. 2014; Sanders et al. 2021; Henry et al. 2021; Li et al. 2023; Langeroodi et al. 2023; Stephenson et al. 2024; Pallottini et al. 2025; Li et al. 2025). Even though metallicity is found to decrease with redshift at a fixed stellar mass, the relation exists across a wide redshift range (up to $z > 6$) with potentially different slopes (e.g., Sanders et al. 2021; Nakajima et al. 2023; Curti et al. 2024; Sarkar et al. 2025; Li et al. 2025). The difference in the metallicities between galaxies in protoclusters or in the fields, however, remains poorly understood. Observations have reported inconsistent conclusions at similar redshifts, and the difference appears to evolve with redshift. Observations of the X-ray cluster XCS2215 ($z = 1.46$) show a metallicity enhancement (i.e., higher 12+log(O/H) at a fixed mass than field

⋆ Corresponding author: xiaohanw78@gmail.com

galaxies at similar redshifts; Adachi et al. 2025). Some observations for $z \sim 2$ protoclusters, such as BOSS1244, reported a metallicity deficit at the high-mass end and enhancement at the low-mass end (Kulas et al. 2013; Kacprzak et al. 2015; Chartab et al. 2021; Sattari et al. 2021; Wang et al. 2022). They suggested that these are consistent with a combination of metal enrichment through feedback and dilution by cold-gas accretion. On the other hand, observations of the Spiderweb protocluster report a metallicity enhancement (Shimakawa et al. 2015; Pérez-Martínez et al. 2023). At higher redshifts ($5 < z < 7$), a recent work showed an enhanced metallicity of ∼0.2 dex for protoclusters on the mass-metallicity relation (Li et al. 2025). Despite these growing efforts, metallicity observations for protoclusters are still limited across a wide range of cosmic time, stellar masses, and galaxy overdensities.

We present the mass-metallicity relation and emission line properties obtained in a field containing the highest overdensity of galaxies and AGNs found so far at $z \sim 3$, the Multi Unit Spectroscopic Explorer (MUSE) Quasar Nebular 01 field (MQN01). MQN01 is a large-scale galaxy overdensity around the $z \sim 3.25$ QSO CTS G18.01. It was first detected as filamentary-shaped Lyα emission structure (Borisova et al. 2016) and was later confirmed by deeper observations (Cantalupo et al., in prep.). MQN01 has been observed by multiwavelength surveys and has shown a high galaxy overdensity and a large fraction of massive galaxies and AGNs with abundant molecular gas (Pensabene et al. 2024; Galbiati et al. 2025; Travascio et al. 2025). MQN01 also contains the largest disk galaxy found so far at $z > 3$, called Big Wheel, with an optical diameter larger than 30 kpc (Wang et al. 2025). We present a study of galaxies detected in the same field using *James Webb* Space Telescope (JWST) Near Infrared Spectrograph (NIRSpec) observations, and we analyze their emission line properties. In Sect. 2 we describe the observations of MQN01. In Sect. 3 we detail the measurements of the galaxy properties and our sample selection. In Sect. 4 we present our main results, that is, the relations between line flux ratios and metallicity versus stellar mass, with comparisons with field galaxies at similar redshifts. In Sect. 5 we discuss possible mechanisms related to environmental effects on metal enrichment, and we present the fundamental metallicity relation. We summarize in Sect. 6. We adopt the AB magnitude system (Oke & Gunn 1983). We adopt a flat ΛCDM cosmology with $H_0 = 67.66\,\mathrm{km\,s^{-1}\,Mpc^{-1}}$, $\Omega_\mathrm{m} = 0.31$, and $\Omega_\Lambda = 0.69$ (Planck 2018, Planck Collaboration VI 2020)[1].

2. Observations and data

Previous multiwavelength observations have provided a multiwavelength view of the MQN01 galaxies, highlighting MQN01 as one of the most overdense protoclusters with a high gas density and AGN fractions (Pensabene et al. 2024; Galbiati et al. 2025; Travascio et al. 2025). The multiwavelength observations altogether have identified a sample of 26 galaxies, 21 of which are MUSE continuum-selected absorption line galaxies, and 5 galaxies are newly uncovered by the Atacama Large (sub)millimeter Array (ALMA) detection. Five of the 26 galaxies are confirmed to have X-ray emission by Chandra observations (Travascio et al. 2025).

The imaging and spectroscopic data we analyzed of the MQN01 field were obtained from *Hubble* Space Telescope (HST) program GO 17065 (PI: Cantalupo), the Very Large Telescope (VLT) program ID 110.23ZX (PI: Cantalupo), and JWST Program GO 1835 (PI: Cantalupo). The photometry includes JWST NIRCam filters F150W2 and F322W2 (Rigby et al. 2023; Rieke et al. 2023), HST filters ACS/WFC F625W and ACS/WFC F814W (Ford et al. 1998), and the High Acuity Wide field K-band Imager (HAWK-I) filters CH4, H, and K_s (Pirard et al. 2004; Casali et al. 2006; Kissler-Patig et al. 2008; Siebenmorgen et al. 2011). Spectroscopic observations, about 8 hours on average, were conducted using the Micro-Shutter Assembly (MSA) observing mode of JWST NIRSpec, with the F170LP/G235H filter and grating pair, covering wavelengths from 1.66 to 3.05 μm at a spectral resolution of $R \sim 2700$. At $z \sim 3.245$, the wavelength coverage corresponds to 3910−7185 Å in rest frame, including key Balmer lines (Hα to Hγ) and metal emission lines (e.g., [OIII] and [NII]; Jakobsen et al. 2022; Böker et al. 2023).

The slits were arranged to cover regions of extended Lyα emission (Borisova et al. 2016, Cantalupo in prep.) on the sky, regardless of previous knowledge of associated galaxies at the redshift of the MQN01 structure. In a very limited number of cases and for locations without extended emission, slits were positioned on known protocluster members, regardless of their stellar mass or SFR. Finally, in some cases, filler slits were located on continuum sources without knowledge of their redshift. The slit design for the MQN01 field is shown in Fig. 1. The spectra for each slit were reduced and combined using the official jwst pipeline (v1.11.3) with the calibration reference file version jwst 1097.pmap. For each slit, the background was modeled by averaging spectra from regions outside of the target galaxy. Spectra near the slit edges were excluded due to noise. The resulting 1D spectra with identified emission lines and composite false-color images are presented in Figs. 2 and B.1. The galaxy redshifts were inferred from the observed wavelengths of Hα and the [OIII]λ5008 lines.

The new JWST/NIRSpec observations complement the existing multiwavelength data of MQN01, providing rest-frame optical spectra with prominent emission lines and thereby extending the available galaxy sample. The construction and properties of the final sample are presented in Sect. 3.2.

3. Measurements and sample selection

3.1. Measurements

3.1.1. Emission line flux

The 1D spectra of the galaxies were extracted from the spatial regions identified in the following way. We determined the galaxy boundary on the slit first by a single-Gaussian fitting to the JWST F322W images, and we then refined it with Hα emission detection. The spectra were integrated within identified galaxy regions.

The emission lines were modeled with single-Gaussian components, with flux ratios fixed at 3.06 for [NII] doublets and 2.94 for [OIII] doublets. The kinematic properties, velocity, and dispersion were assumed to be the same for the [OIII] doublets or Hα + [NII] doublets. The stellar continuum, which is substantially weaker than the emission lines for our sample, was removed by a linear fitting of the continuum region around the emission lines of interest. For one galaxy with broad emission line features (ID: 3001, shown in the top panel of Fig. 2), the emission lines were modeled with two Gaussian components (one additional component for Hα and the [NII] doublets). The

[1] All cosmological calculations in this work are performed using the `Planck18` cosmology implemented in the `astropy.cosmology` package (Astropy Collaboration 2022).

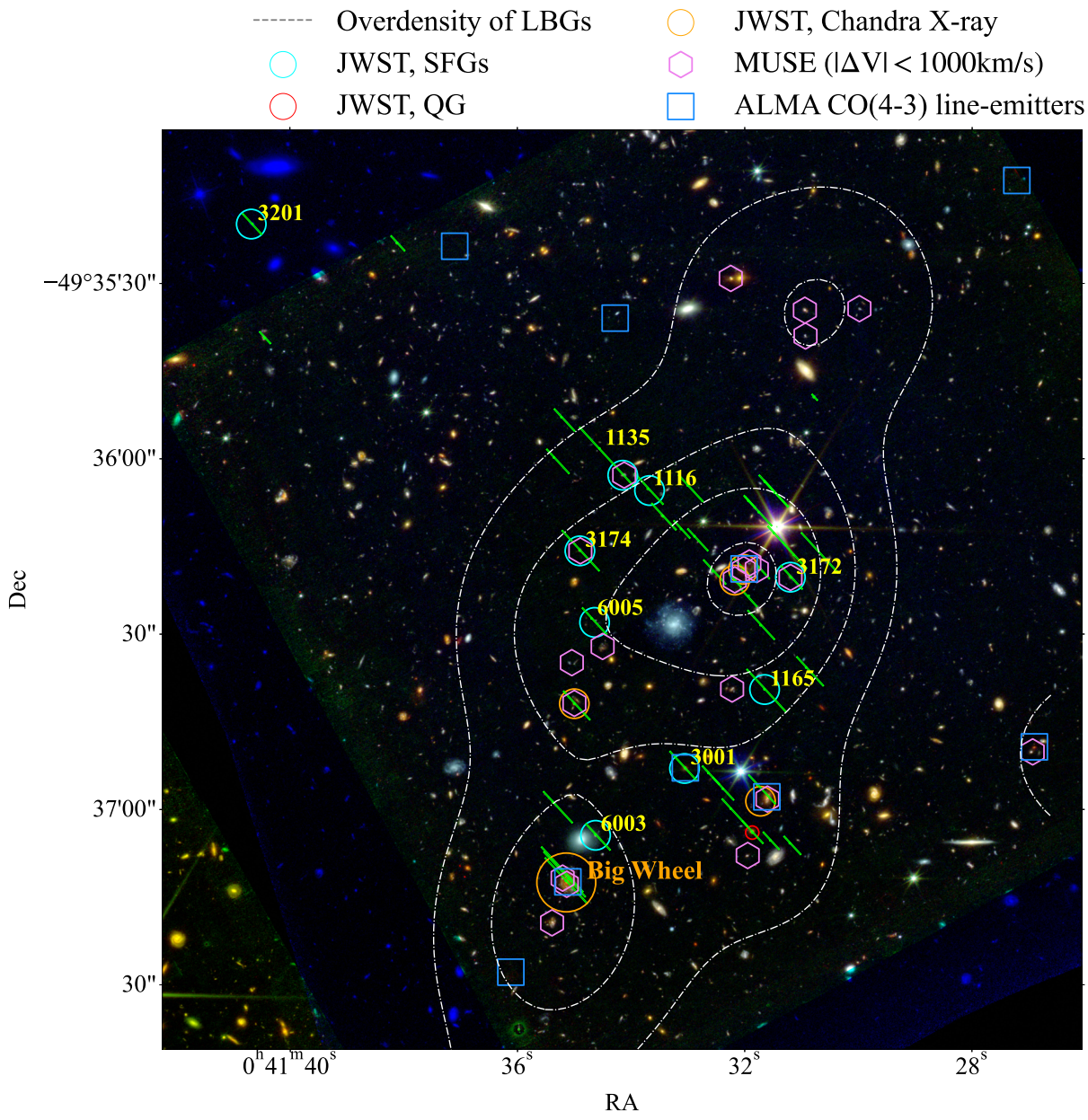

Fig. 1. Slit design of the JWST program GO 1835 (PI: Cantalupo) targeting the MQN01 protocluster field (see text for details of the slit location selection). The composite false-color image of the field was created with HST F814W (0.8 μm; blue), JWST F150W2 (1.5 μm; green), and JWST F322W2 (3.2 μm; red). The JWST/NIRSpec slit apertures are indicated by green rectangles. The dashed contours show the galaxy overdensity (Galbiati et al. 2025). The distribution of samples identified from MUSE observations (Galbiati et al. 2025), Chandra X-ray observations (Travascio et al. 2025), and ALMA (Pensabene et al. 2024) are also included. The sample of identified star-forming galaxies detected with emission lines is marked with cyan circles. Galaxies with X-ray emission are marked as orange circles. A quiescent galaxy serendipitously found with the JWST NIRSpec observations (Wang et al. 2026) is marked with a red circle.

flux of the narrow Gaussian components was adopted in the analysis for galaxy 3001.

3.1.2. Stellar mass

We derived the stellar masses through a spectral energy distribution (SED) fitting with CIGALE v2025.0 (Burgarella et al. 2005; Noll et al. 2009; Boquien et al. 2019), using photometry from HST F814W, F625W, and F160W, HAWK-I K_s, and JWST F150W2 and F322W2. For one galaxy that was not observed by JWST/NIRCam (ID: 3201), we used photometry from HST F814W, HAWK-I H, CH4, and K_s. A delayed-τ star formation history (SFH) with a high fixed value of $\tau = 100$ Gyr was assumed, together with a Chabrier (2003) initial mass function, Bruzual & Charlot (2003) stellar population synthesis models, and the Calzetti et al. (2000) dust attenuation law. The stellar and nebular metallicities were fixed to solar metallicity (0.02). The input parameters in the SED fitting are summarized in Table 1. We adopted the median (50th percentile) stellar mass of the Bayesian posterior distribution in log space and uncertainties defined by the 16th–84th percentile range.

To address the robustness of stellar mass estimates, we performed a series of SED fittings with CIGALE, including different star formation histories (with and without bursts),

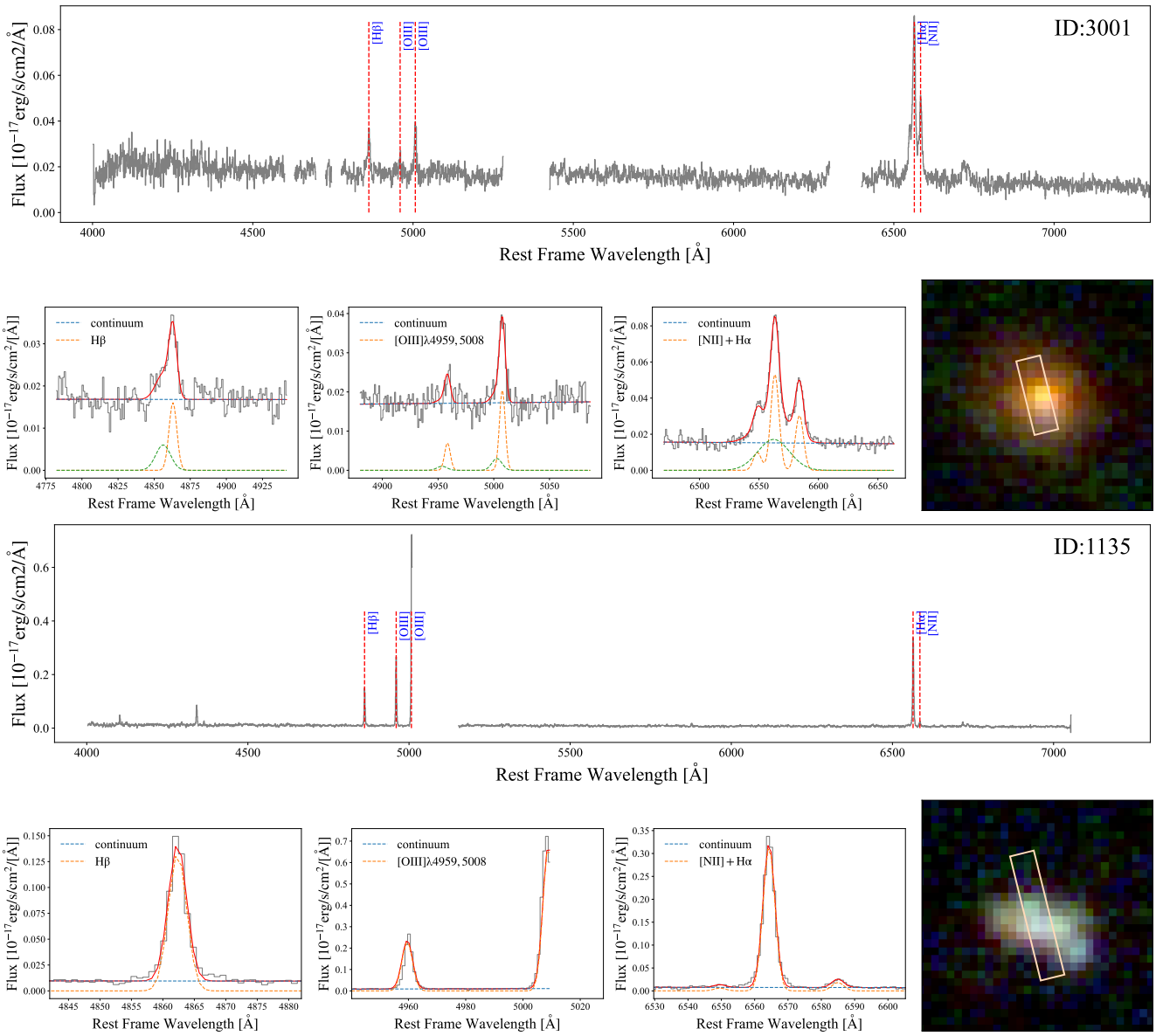

Fig. 2. Integrated 1D spectra and composite false-color images of two galaxies in the sample, with slit IDs 3001 and 1135. The flux density is given in unit of 10^{-17} erg/s/cm^2/Å, and the wavelength is given in rest-frame Angstroms. The slit regions from which the 1D spectra were extracted are overplotted on the galaxy images as light pink boxes. The emission lines were modeled with single Gaussians. For galaxy 3001, which shows broad emission line features, an additional Gaussian component was included (shown by the dotted green line). The flux of the narrow Gaussian components was adopted in the analysis for galaxy 3001. The filters used to create the color images are HST F814W (0.8 μm; blue), JWST F150W2 (1.5 μm; green), and JWST F322W2 (3.2 μm; red). The spectra and images for the remaining galaxies are given in Fig. B.1.

metallicities (with $Z_* = Z_{\rm gas}$), nebular parameters (ionization parameter $\log U$ and electron density n_e), and grid setups for the star formation history parameters. The stellar masses remain broadly consistent. In addition, we also carried out runs without nebular emission to provide conservative upper limits on the stellar mass, which showed consistent results. We also tested a combination of $Z_* = 0.004$[2] and the Small Magellanic Cloud (SMC) extinction curve (Gordon et al. 2003), which was suggested for high-redshift and low-metallicity galaxies (Reddy et al. 2018; Du et al. 2018; Shapley et al. 2023b). The derived stellar masses are somewhat lower than the combination of solar metallicity and Calzetti et al. (2000) extinction, while the differences are small and do not affect our main conclusions. We adopted the masses derived with a configuration similar to that commonly used in the literature, especially for better consistency with the datasets of the reference field galaxy (Sanders et al. 2021; Li et al. 2023). Figures using $Z_* = 0.004 +$ SMC stellar masses are shown in Appendix C for reference.

3.1.3. Star formation rate

The SFR is measured from integrated Hα flux, corrected for aperture effects and dust attenuation. We used

$$\mathrm{SFR}\,[\mathrm{M}_\odot\,\mathrm{yr}^{-1}] = 10^{-41.35} \times L_{\mathrm{H}\alpha}\,[\mathrm{erg/s}], \quad (1)$$

assuming a Chabrier (2003) IMF (Hao et al. 2011). The distribution of the sample on the star formation main sequence (SFMS) is presented in Fig. 4.

[2] Referred to "0.27 $Z_\odot$ + SMC" in Reddy et al. (2018), Shapley et al. (2023b), where $Z_\odot = 0.014$.

Table 1. Input parameters for the SED-fitting code CIGALE.

Parameter	Value
	sfhdelayed
τ	100 Gyr
Age	20, 30, 40, 50, 65, 80, 95, 110, 130, 150, 170, 200, 230, 260, 300, 350, 400, 460, 520, 600, 680, 760, 840, 920, 1000, 1100, 1200, 1350, 1500, 1650, 1800, 1900 (Myr)
$f_{\rm burst}$	0.0
	bc03
imf	1 (Chabrier)
metallicity	0.02
seperation_age	10 Myr
	nebular
logU	−3.8, −3.2, −2.6, −2.0, −1.5
zgas	0.02
ne	100
$f_{\rm esc}$	0.0
$f_{\rm dust}$	0.0
lines_width	500.0 km/s
	dustatt_calzleit
E_BVs_young	0.00, 0.05, 0.1, 0.15, 0.2, 0.25, 0.30, 0.45
E_BVs_old_factor	0.44
uv_bump_amplitude	0.0
powerlaw_slope	0.0
filters	galex.FUV & generic.bessell.B & generic.bessell.V

It has been shown that galaxies with low metallicities tend to produce more Hα emission at the same SFR, with the conversion factor increasing with metallicity (Korhonen Cuestas et al. 2025). A lower conversion factor might be suggested for high-redshift galaxies with lower stellar masses and lower metallicities (Shapley et al. 2023b). We also calculated the SFR using SFR[$M_\odot$ yr^{-1}] = $10^{-41.64} \times L_{\rm H\alpha}$ [erg/s], which was derived from low-metallicity BPASS models (Theios et al. 2019), To maintain consistency with the datasets of the reference field galaxy (Sanders et al. 2021; Li et al. 2023), we adopted a conversion factor of $10^{-41.35}$ throughout the analysis. Figures using the lower conversion factor, combined with $Z_* = 0.004 + {\rm SMC}$ stellar masses (see Sect. 3.1.2), are shown in Appendix C for reference.

To correct for slit loss, we performed rectangular aperture photometry over the slit-covered region of each galaxy and calculated the ratio of the galaxy flux falling within the slit region used to extract the spectrum and the total galaxy flux. Aperture correction factors were calculated using F322W2 and F150W2, and were applied separately to the Hα and Hβ fluxes. For the galaxy that was not covered by the JWST/NIRCam observations (ID: 3201), we estimated the correction using the HST F814W image. The central wavelength of F814W is much shorter than the redshifted Hα wavelength and might lead to an underestimation. However, the image resolution of HST is also lower than that of the JWST, leading to an overestimation, conversely. We simply adopted this value for the aperture correction for this galaxy and note this in figure captions and following texts. Hα and Hβ were corrected using the same factor for this galaxy.

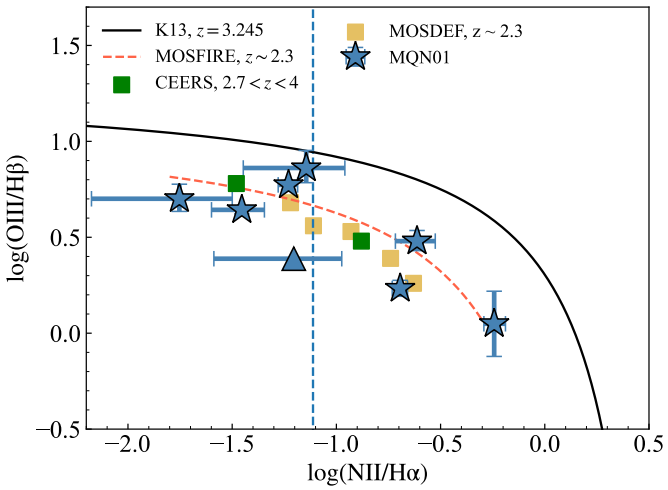

Fig. 3. Baldwin-Phillips-Televich diagram for the MQN01 galaxy sample. The classification curve is from Kewley et al. (2013) with z = 3.245. Galaxies are shown as blue stars. For one galaxy (ID: 6005) without an Hβ detection, a 3σ upper limit is adopted, resulting in a lower limit for [OIII]λ5008/Hβ, shown as a blue triangle. The galaxy whose [OIII] falls within the spectrum detection gap (ID: 3201, see Fig. B.1) is shown as the vertical dashed line at its [NII]λ6585/Hα value. The distribution of the stacked CEERS 2.7 < z < 4.0 sample (Shapley et al. 2023a), stacked MOSDEF $z \sim 2.2$ (Sanders et al. 2021), and the best-fit relation for the KBSS-MOSFIRE sample at $z \sim 2.3$ (Steidel et al. 2014) are also included.

The SFR was dust-corrected with Cardelli et al. (1989) law assuming an intrinsic Balmer decrement of 2.79. For the galaxy (ID: 6005) whose Hβ was too faint to be detected, we were unable to correct for the dust attenuation based on the Balmer decrement. Therefore, we adopted its uncorrected SFR as a lower limit.

3.1.4. Gas-phase metallicity

The gas-phase metallicity was derived using calibrations in Bian et al. (2018), with emission line diagnostics, N2 (log [NII]λ6585/Hα), O3 (log [OIII]λ4959, 5008/Hβ) and O3N2 (log(([OIII]λ5008/Hβ)/([NII]λ6585/Hα))), following the empirical relations

$$\mathrm{N2} = (x - 8.82)/0.49, \tag{2}$$

$$\mathrm{O3} = 43.9836 - 21.6211x + 3.4277x^2 - 0.1747x^3, \tag{3}$$

$$\mathrm{O3N2} = (8.97 - x)/0.39, \tag{4}$$

where x = 12 + log(O/H). We adopted the Bian et al. (2018) calibrations for consistency with measurements of the reference field galaxy (Sanders et al. 2021; Li et al. 2023).

We followed Sanders et al. (2021) and derived the metallicities by minimizing

$$\chi^2 = \sum_i \frac{(R_{{\rm obs},i} - R_{{\rm cal},i})^2}{\sigma^2_{{\rm obs},i} + \sigma^2_{{\rm cal},i}}, \tag{5}$$

where $R_{\rm obs}$ is the observed line ratio, $R_{\rm cal}$ is the line ratio predicted by each calibration with a given metallicity, $\sigma_{\rm obs}$ is the uncertainty of the line ratio, and $\sigma_{\rm cal}$ is the dispersion of each calibration. As Bian et al. (2018) fit stacked spectra and provided no measured calibration scatters, we followed Sanders et al. (2021) and adopted the mean of values from the literature

(Maiolino et al. 2008; Jones et al. 2015; Curti et al. 2017), with $\sigma_{\rm cal,N2} = 0.15$, $\sigma_{\rm cal,O3} = 0.10$, and $\sigma_{\rm cal,O3N2} = 0.16$. The Bian et al. (2018) calibrations were extrapolated to $7.8 < 12 + \log({\rm O/H}) < 8.8$ ($7.8 < 12 + \log({\rm O/H}) < 8.4$ for the sample in Bian et al. 2018) to cover the high-mass galaxies in the MQN01 sample. For galaxies with undetected Hβ or [NII] or where [OIII] fell within a spectral coverage gap (see ID: 3172 in Fig. B.1), only the available diagnostic was used. We generated 1000 realizations of the emission line fluxes for each galaxy and adopted the median value of the resulting distribution, with uncertainties from the 16 and 84 percentile.

3.2. Sample and comparison with previous observations and field galaxies

We verified the emission line features for all slit spectra and identified 15 galaxies with clear emission detections within ~1500 km/s relative to the central QSO. Eight of the 15 galaxies have been identified in the MUSE-selected sample (Galbiati et al. 2025), and 5 of the 15 have X-ray emission (Travascio et al. 2025). One of the 10 galaxies without an X-ray detection has a suppressed SFR (~1 dex below the SFMS based on conservative SFR estimates from Hα or UV), with strong Balmer and metal absorption lines, and it was thus classified as quiescent and excluded from our sample (Wang et al. 2026). Because of the known complications in the gas excitation mechanisms with AGNs and the resulting uncertainties in metallicity measurements, AGN hosts were excluded from the sample for the analysis. We finally identified a sample of 9 star-forming galaxies (SFGs). The distribution of the parent (15 galaxies) and identified (9 galaxies) sample is shown as colored circles in Fig. 1. The distribution of our final star-forming sample on the BPT diagram (Baldwin et al. 1981) is shown in Fig. 3, falling into the star-forming HII regions classified by Kewley et al. (2013) at $z \sim 3.25$, which is broadly consistent with previous studies of galaxies at redshifts of 2–4 (Steidel et al. 2014; Sanders et al. 2021; Shapley et al. 2023b).

We note that the BPT diagram and BPT-based AGN classification may become unreliable at higher redshifts: lower metallicities at high z may cause AGNs to overlap with the SF regions (e.g., Groves et al. 2006; Nakajima & Maiolino 2022; Übler et al. 2023; Kocevski et al. 2023; Richardson et al. 2025; Cleri et al. 2025). Our SFG sample selection was primarily based on X-ray emission observations to exclude galaxies with clear AGN signatures. Broad-line features are widely adopted to identify hidden AGNs (e.g., Übler et al. 2023; Kocevski et al. 2023; Greene et al. 2024). Our SFG sample generally exhibits narrow emission lines, with one exception, galaxy ID 3001, which shows broad emission lines, as shown in Fig. 2.

For ID 3001, we observe a kinematically distinct broad component (full width at half maximum, FWHM, ~1400 km/s for Hα and ~740 km/s for Hβ, with blueshifted velocity offsets). These FWHMs are smaller than those of the typical broad-line AGNs (e.g., Hao et al. 2005; Greene et al. 2024) and more indicative of a strong galactic outflow. While these velocities might suggest an AGN-driven outflow (given its modest current SFR), our ultra-deep X-ray data for 3001 show no signs of currently ongoing AGN; this outflow might be driven by a past AGN or a past starburst episode. Furthermore, the absence of X-ray emission combined with a moderate Balmer decrement (Hα/H$\beta \sim 4$, corresponding to $A_V \sim 1.1$) makes a heavily obscured AGN unlikely. We emphasize that our metallicity measurements used the narrow-line components. The lack of an X-ray detection and the star-forming nature of the narrow-line BPT ratios confirm that these narrow lines trace the host galaxy HII regions, which are kinematically and physically decoupled from the outflowing gas. Given the lack of definitive AGN evidence and the robustness of the narrow-line metallicity, we retained this source to maintain the statistical integrity of our high-mass sample.

In the final sample of SFGs, three of nine were included in the MUSE-selected sample, and one of the remaining six was included in the ALMA sample. The distribution of the MQN01 JWST sample on the star formation main sequence is presented in Fig. 4, with the MUSE-selected sample plotted for comparison. Compared to the MUSE sample, the MQN01 sample extends toward lower stellar masses and systematically lower SFRs, while the specific SFRs (sSFRs) remain comparable. This is due to the high fraction of AGNs at the high-mass end in the MQN01 field (Travascio et al. 2025), whereas AGNs were excluded in this work. For star-forming galaxies with $M < 10^{10.5}\,M_\odot$, the two samples are broadly consistent.

To place the MQN01 sample into context, we also compared the MQN01 sample with several widely used SFMS relations and other samples at similar redshifts, as shown in Fig. 4. We adopted the parameterizations of SFMS from Speagle et al. (2014) and Popesso et al. (2023) as general benchmarks and included the field-galaxy samples at similar redshifts from Sanders et al. (2021) and Li et al. (2023) for a direct observational comparison. The SFRs of the MQN01 SFGs are comparable to those of the reference SFMSs.

4. Line ratios and metallicity versus stellar mass of MQN01

In this section, we present our main results on the chemical properties of the MQN01 star-forming galaxy sample. Specifically, we focus on the emission line ratios and the gas-phase metallicity.

4.1. Line ratios

We began by investigating the relations between emission line ratios and stellar masses. Figure 5 shows [NII]λ6585/Hα and [OIII]λ5008/Hβ versus stellar mass for the MQN01 sample. The galaxy without an Hβ detection (ID: 6005) is plotted as a triangle with 3σ upper limit of Hβ in the right panel of Fig. 5. For comparison, we include the relations for field galaxies at similar redshifts. We include the stacked CEERS sample (Shapley et al. 2023a) for [NII]λ6585/Hα], as observations at $z > 3$ are rare due to limited wavelength coverage, and we include the samples from Onodera et al. (2016), Sanders et al. (2021) and Li et al. (2023) for [OIII]λ5008/Hβ, which is more available at $z > 3$.

In the MQN01 sample, [NII]λ6585/Hα increases while [OIII]λ5008/Hβ decreases with stellar mass. [NII]λ6585/Hα and [OIII]λ5008/Hβ serve as metallicity indicators. [NII]λ6585/Hα increases with metallicities, while [OIII]λ5008/Hβ first increases and then decreases with metallicity when $12 + \log({\rm O/H}) \gtrsim 8$ (Maiolino et al. 2008; Curti et al. 2017; Bian et al. 2018; Sanders et al. 2020). This metallicity regime is a reasonable estimate for our sample given its stellar mass range. Therefore, the observed trends of the two flux ratios are consistent with a metallicity increase toward higher stellar masses. This is consistent with the well-established mass-metallicity relation.

Compared with field galaxies at similar redshifts, the MQN01 galaxies cover a similar range in each emission line ratio, but show a systematic offset toward higher metallicities (higher [NII]λ6585/Hα and lower [OIII]λ5008/Hβ). This is

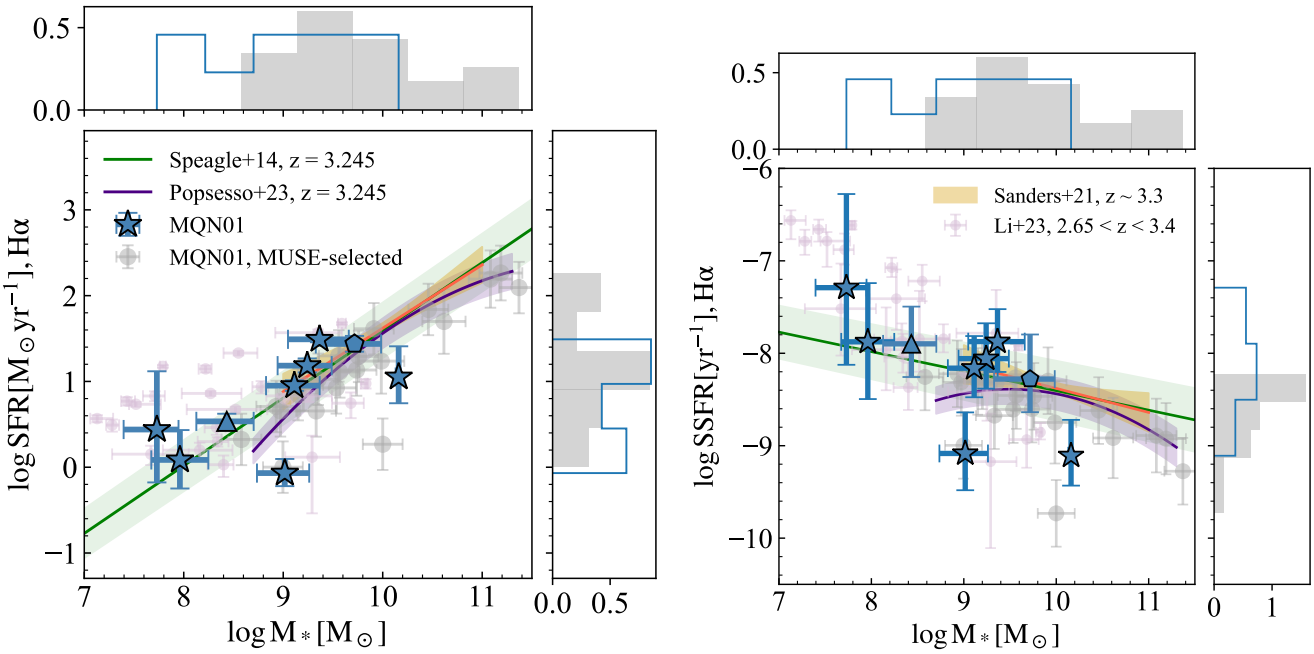

Fig. 4. Star formation rate and sSFR vs. stellar mass for the MQN01 sample. The SFR is calculated by Hα emission with aperture and dust correction. The galaxy sample is shown as blue stars. For the galaxy without an Hβ detection (ID: 6005), the SFR uncorrected for dust attenuation is adopted as a lower limit, shown as a blue triangle. For the galaxy without JWST photometry (ID: 3201), aperture correction calculated from HST F814W is adopted and is shown as a blue pentagon. The SFR and stellar mass derived from SED fitting for a larger sample of MQN01 galaxies (Galbiati et al. 2025) are shown as gray circles. The histograms at the top and right in both panels show the distribution of the SFR, SSFR and stellar mass for MQN01 sample in this work (blue) and that from Galbiati et al. (2025, gray). For comparison, the best-fit SFR–M_* relation for the MOSDEF sample with median $z \sim 3.3$ (Sanders et al. 2021) is shown as the orange line, with the shaded region indicating the 1σ uncertainty of the fitting parameters. The SFR and SSFR versus stellar mass from Li et al. (2023) are shown as purple circles. The SFR and SSFR–M_* from Speagle et al. (2014) and Popesso et al. (2023) at $z = 3.245$ are shown as green lines and purple lines, with 1σ uncertainties of the fitting parameters shown as the shaded regions. Compared with reference SFMS, the MQN01 sample shows a median offset of ~0.05 dex above the referred star formation main sequence (Speagle et al. 2014).

clearer at $\log M_*/M_\odot > 9$, where MQN01 galaxies consistently tend to lie above the [NII]/Hα and below the [OIII]/Hβ values of stacked spectra from Shapley et al. (2023a) and Sanders et al. (2021) at fixed mass. At $\log M_*/M_\odot < 9$, there is no direct comparison with field galaxies for [NII]λ6585/Hα and limited datasets for [OIII]λ5008/Hβ. The MQN01 galaxies tend to lie above the extrapolated [NII]/Hα–mass relation from Shapley et al. (2023a) at $\log M_*/M_\odot < 9$, while their [OIII]/Hβ ratios are broadly consistent with the measurements of Li et al. (2023). Because the statistics at the low-mass end are limited, it remains difficult to draw firm conclusions for the full mass range. Nevertheless, the overall trend suggests that MQN01 star-forming galaxies tend to have relatively higher metallicities than their field counterparts, especially at the high-mass end.

4.2. Mass-metallicity relation

We present the mass-metallicity relation (MZR) for the MQN01 sample in Fig. 6, offering one of the first views of the MZR for protocluster galaxies at $z \sim 3$. For comparison, we include reference results for field galaxies from Sanders et al. (2021) and Li et al. (2023), which are shown as median trends and individual data points. We also include the metallicity for the binned spectra of CEERS at $2.7 < z < 4.0$, with N2, O3, and O3N2 from Shapley et al. (2023a), calculated in the same way as for the MQN01 sample. We modeled the mass-metallicity relation of the MQN01 sample with a linear form,

$$12 + \log(\mathrm{O/H}) = k(\log M_* - \log M_0) + Z_0, \quad (6)$$

where $\log M_0$ is the mean mass weighted by the inverse variance of the metallicities. We obtained the best-fit relation with 1σ uncertainties with the full sample using an MCMC fitting,

$$12 + \log(\mathrm{O/H}) = (0.32 \pm 0.08) \times (\log M_* - 9.45) + (8.52 \pm 0.06). \quad (7)$$

The MQN01 sample shows a clear increasing metallicity trend versus stellar mass with a best-fit slope of $k = 0.32 \pm 0.08$. Compared with the reference data, the MQN01 galaxies show higher metallicities at fixed stellar mass on average, which is consistent with the flux ratios in Fig. 5. To evaluate the average difference between our sample and the field galaxy samples, we implemented a Monte Carlo (MC) resampling procedure with 10^4 iterations, incorporating observational errors and fitting uncertainties. The data points were sampled using either Gaussian or split-normal distributions, depending on the symmetry of their error bars. In each iteration, a synthetic dataset was generated by perturbing the X and Y coordinates of all data points and the model parameters. The final mean difference and its 1σ uncertainty were derived from the mean and standard deviation of the resulting distribution. At $\log M_*/M_\odot > 9$, the MQN01 galaxies show a mean offset of 0.17 ± 0.04 dex above to the median relation presented from Sanders et al. (2021). At $\log M_*/M_\odot < 9$, the distribution of MQN01 metallicities is closer to that of the Li et al. (2023) sample, with a mean offset of only 0.03 ± 0.09 dex. The latter difference is modest and statistically insignificant within 1σ uncertainties.

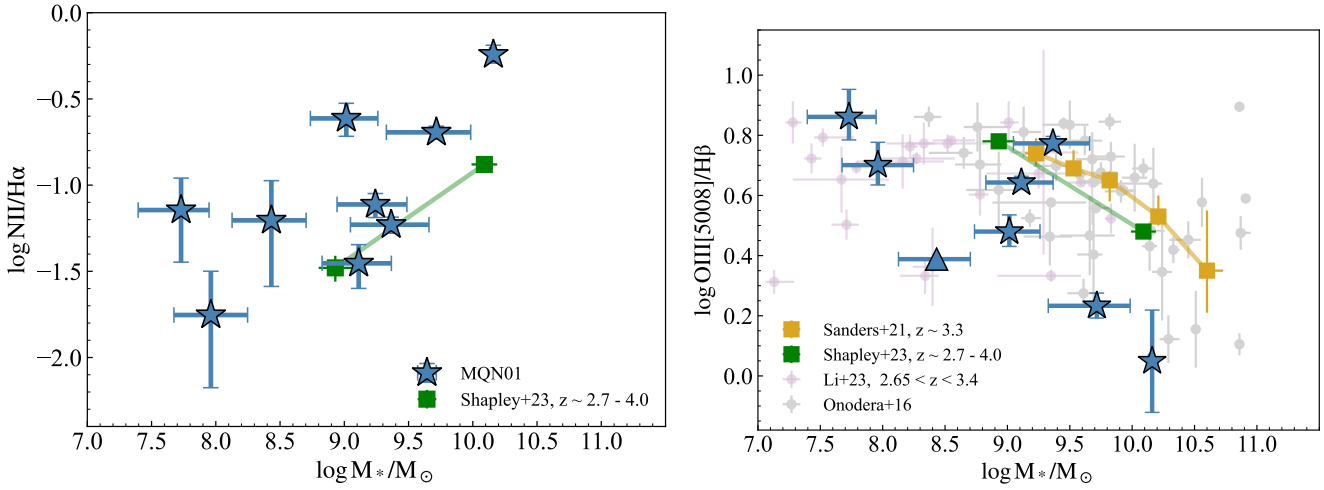

Fig. 5. Emission line flux ratio vs. stellar mass for the MQN01 sample. The sample is marked as blue stars. Left: log [NII]λ6585/Hα vs. stellar mass. Reference data from stacked spectra of the CEERS sample with $2.7 < z < 4.0$ (Shapley et al. 2023a) are shown as green squares. Right: log [OIII]λ5008/Hβ vs. stellar mass. The galaxy without an Hβ detection is shown as a triangle at the lower limit of [OIII]λ5008/Hβ based on the 3σ detection. The datasets from Onodera et al. (2016), Sanders et al. (2021), Li et al. (2023), Shapley et al. (2023a) are included for comparison. The individual data points are shown as filled circles, with stacked values shown as squares.

For statistical comparison with field galaxies, whose samples cover different mass ranges, we also fit the galaxy sample subsets with the same mass coverage as the field galaxy samples. The best-fit relations with uncertainties for the MQN01 sample and for reference relations are shown in Fig. 7, and the best-fit parameters are summarized in Table 2. Compared with Sanders et al. (2021), the best-fit MZR of the MQN01 full sample has a consistent slope ($\Delta k = 0.03 \pm 0.08$) and a systematic offset of 0.26 ± 0.07 toward higher metallicity at $\log M_{\rm ref} = 10$. Restricted to $\log(M_*/M_\odot) > 9$, the MQN01 slope is slightly steeper with similar offsets. We note that the offset at the specific reference point is larger than the mean residual because the slope of the best-fit relation is steeper than the reference relation. When compared with Li et al. (2023) and restricted to the range of $7.5 < \log(M_*/M_\odot) < 10$, the best-fit relation shows a larger scatter. The average offset remains toward higher metallicity (0.07 ± 0.27) with consistent slopes ($\Delta k = -0.01 \pm 0.16$), while the significance is below 1σ. The statistical analysis suggests a systematic metallicity excess in the MQN01 galaxies relative to the field galaxy samples. This is most pronounced at the high-mass end. At lower masses, a similar tendency is present, but the significance is limited.

We also examined the effect of the metallicity calibration methods to which the MZR measurements might be sensitive. We adopted the Bian et al. (2018) calibration for consistency with the reference data. However, the specific set of emission line diagnostics might vary between samples because the wavelength coverage and data quality are different. To investigate the potential effect of these differences, we calculated metallicities for the Sanders et al. (2021) and Li et al. (2023) samples with O3, which is the only available line ratio that overlaps what we used here. The recalculated mass-metallicity relations are shown in Fig. 8. For the Sanders et al. (2021) sample, the O3-based metallicities are highly consistent with the published values with a slight offset. For the Li et al. (2023) sample, however, the recalculated metallicities reach higher values, and the measurements from the stacked spectra even show a decreasing trend with stellar mass, which is inconsistent with the well-established MZR. This might reflect methodological details in the stacking procedure and is beyond the scope of this work. As an additional cross-check, we derived binned O3 metallicities by summing the reported line fluxes. These values, shown as purple triangles in Fig. 8, are more consistent with the established MZR, but lie systematically above the published relation of Li et al. (2023), and they show no clear difference from the MQN01 distribution. We also note that the scatter of the O3-based metallicities for the Li et al. (2023) sample is larger than that of the published values. The inconsistencies between the O3-based and published metallicities might indicate the limited constraining power of O3 on metallicities or uncertainties in measuring weak Hβ emission, while a detailed assessment is beyond the scope of this work. Overall, these O3-based recalculations provide a sanity check, while in the following, we adopt the published relations in Fig. 6 as the common reference for statistical comparison in order to remain directly comparable with earlier work.

5. Discussion

5.1. Environmental effect on the metal enrichment

In the previous sections, we have shown the mass-metallicity relation for the MQN01 sample. The MQN01 galaxies show a tendency toward higher metallicities than field galaxies, especially at higher masses, with less significance at low mass. These differences might indicate environmental effects on the metal enrichment with mass dependence.

Previous observations have suggested that galaxies in the overdense environments may assemble their stellar mass more rapidly or at earlier times than field galaxies (Galbiati et al. 2025). The earlier star formation in protoclusters therefore leads to earlier metal enrichment, while field galaxies experience a more delayed metal enrichment. This is consistent with the high fraction of massive galaxies and AGN in MQN01, which indicates accelerated growth. Other mechanisms, such as gas stripping and galaxy interactions that lead to metal-poor gas loss and metal enhancement, may also play a role. However, they would be expected to enhance metallicities especially in low-mass systems, which is not observed here. We also note that the slopes of the MZR of MQN01 given by fitting within different mass regions are consistent with the reference field galaxies, which

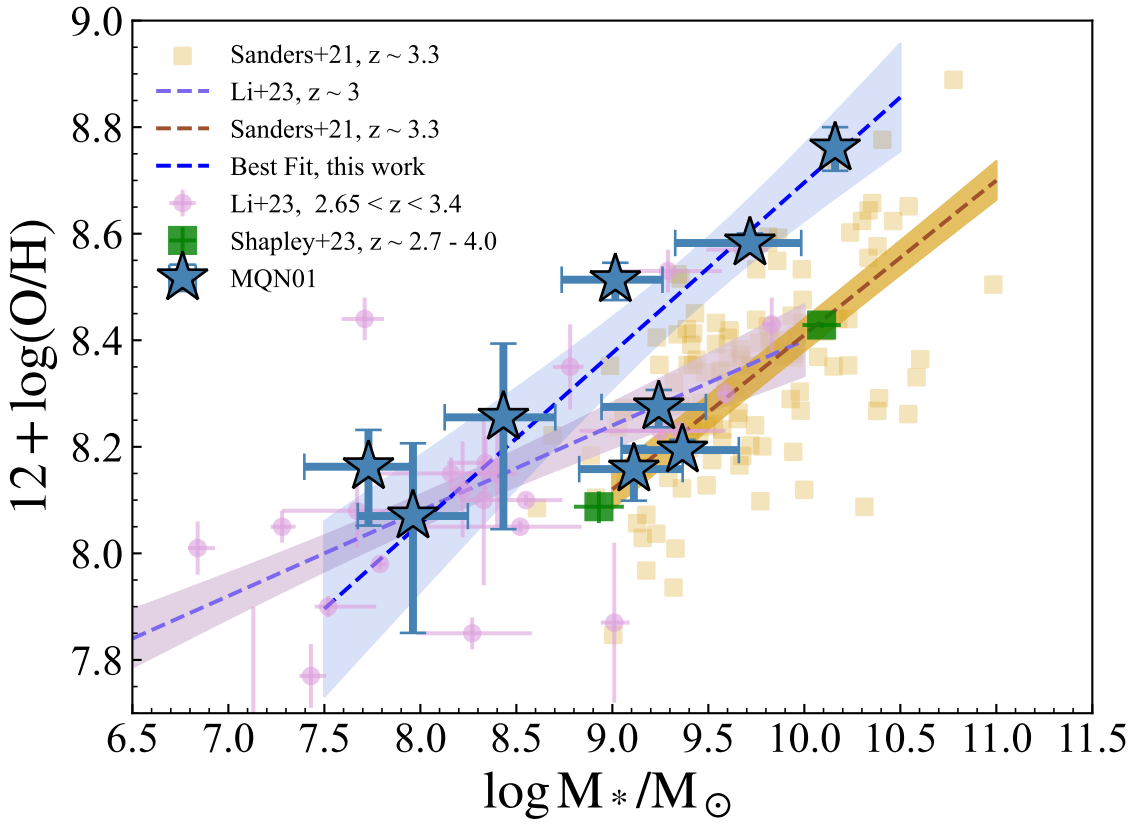

Fig. 6. Mass-metallicity relation for the MQN01 sample. The MQN01 galaxies are shown as blue stars. The best-fit relation with 1σ uncertainties of the total MQN01 sample is shown as a blue line and shaded region. The reference datasets at similar redshifts from Sanders et al. (2021), Li et al. (2023) are included, where the individual galaxies are shown as filled circles and squares, with the best-fit relations shown in lines and shaded regions representing 1σ uncertainties. The individual data points of the sample in Sanders et al. (2021) were extracted using WebPlotDigitizer. The CEERS sample (Shapley et al. 2023a) is shown as green squares, with metallicities calculated using N2, O3, and O3N2 with Bian et al. (2018) calibrations.

might suggest that the environmental effects primarily shift the normalization rather than the shape of the relations at $z \sim 3$. At low masses, the slope of MZR is shallower than that of the high-mass end, which might be due to different feedback mechanisms at different mass ranges (Davé et al. 2011; Li et al. 2023). However, when the full sample was fit, the slope was steeper and more consistent with the MZR for massive galaxy samples. The current sample is still quite limited, and further observations are therefore required to better constrain the low-mass regime and to establish whether the environment leaves a robust imprint on the MZR at $z \sim 3$.

Observations of protoclusters at $z > 3$ are still sparse. As summarized in Sect. 1, observations have reported inconsistent results at $z \sim 2$. Some have reported a metallicity deficit at the high-mass end and an enhancement at the low-mass end, which were interpreted as a combined effect of metal enrichment through feedback and dilution by cold-gas accretion (Kulas et al. 2013; Kacprzak et al. 2015; Chartab et al. 2020; Sanders et al. 2021; Wang et al. 2022). Some other observations have reported metallicity enhancement that was interpreted as suppressed cold-gas supply by shock-heated protocluster halos and more efficient metal-enriched gas recycling (Shimakawa et al. 2014, 2015; Pérez-Martínez et al. 2023). At higher redshifts, $5 < z < 7$, Li et al. (2025) reported a metallicity enhancement in protoclusters.

We stress, however, that different systems are identified as protoclusters based on different criteria, and, in some cases, even modest overdensities on large scales are considered protoclusters in the literature. The observations and analysis of MQN01 add to the limited observational constraints on the MZR of protocluster galaxies at $z \sim 3$ for a system that shows the highest overdensity in terms of continuum-selected star-forming galaxies, CO emitters, and AGN, at least in the central area of 4 arcmin^2 covered by JWST observations and ALMA (Galbiati et al. 2025; Pensabene et al. 2024; Travascio et al. 2025). Unfortunately, different galaxy selections in different fields hamper the possibility of a detailed comparison based on overdensities.

The higher metallicities seen in MQN01 might suggest that metallicity enhancement is still present above a given overdensity of galaxies at $z \sim 3$. Further observations of protoclusters across a wider range of overdensities and redshifts is essential to further understand the environmental effect on MZR and its redshift evolution.

5.2. The fundamental metallicity relation

In this subsection, we further investigate the fundamental metallicity relation (FMR), which combines stellar mass and star formation. In the local universe, the MZR has been found to have a secondary dependence on SFRs, where galaxies with higher SFRs tend to exhibit lower gas-phase metallicities at fixed stellar masses. This trend is referred to as the fundamental metallicity relation (FMR; e.g., Ellison et al. 2008; Lara-López et al. 2010; Mannucci et al. 2010; Yates et al. 2012; Curti et al. 2020;

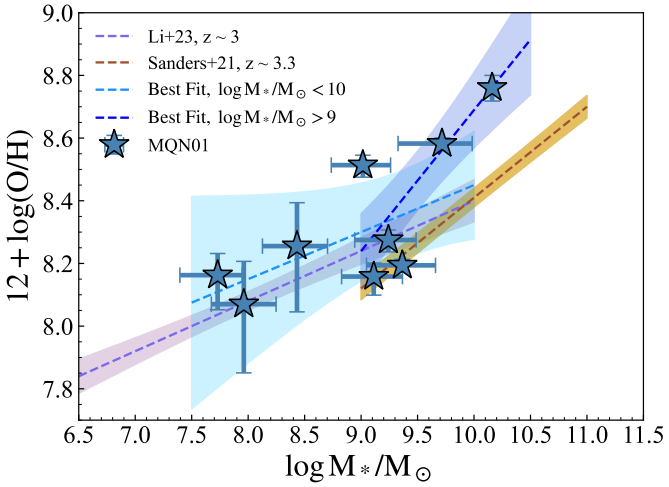

Fig. 7. Best-fit relations with 1σ uncertainties of the MQN01 sample with $\log M_*/M_\odot < 10$ and $\log M_*/M_\odot > 9$ for consistency with the mass range of Li et al. (2023) and Sanders et al. (2020).

Sanders et al. 2021; Sarkar et al. 2025). The FMR is physically in line with gas-regulator models, arising from the balance among galaxy gas fraction, metal content, and stellar mass (Tremonti et al. 2004; Davé et al. 2011, 2012; Lilly et al. 2013). At higher redshifts, the FMR has been found to exist out to $z \sim 2.5$ (Sanders et al. 2018; Cresci et al. 2019; Curti et al. 2020; Sanders et al. 2021), while its existence and possible evolution along redshifts remain to be investigated (Troncoso et al. 2014; Onodera et al. 2016; Sanders et al. 2021; Nakajima et al. 2023; Curti et al. 2024; Sarkar et al. 2025; Li et al. 2025). The FMR is parameterized as a function of μ_α instead of mass, where $\mu_\alpha = \log M_*/M_\odot - \alpha \log(\mathrm{SFR}[\mathrm{M}_\odot\,\mathrm{yr}^{-1}])$ (Mannucci et al. 2010). The value of α varies among different samples at different redshifts (e.g., Mannucci et al. 2010; Andrews & Martini 2013; Guo et al. 2016; Curti et al. 2020; Sanders et al. 2021). For a better comparison with field galaxy samples, we simply adopted the value of $\alpha = 0.60$ from Sanders et al. (2021). The resulting FMR is shown in Fig. 9. As in Figs. 4 and 5, the galaxy without an Hβ detection (ID: 6005) is marked as a triangle with an upper limit of $\mu_{0.60}$, and the galaxy with no JWST photometry (ID: 3201) is marked as a pentagon. The MOSDEF sample is included for comparison and is shown as brown squares. The FMR fitted with a $z \sim 0$ sample presented in Sanders et al. (2021) is shown as the dashed curve. Sanders et al. (2021) has pointed out that the FMR depends weakly on redshift. The distribution of MOSDEF samples with $z \sim 2.3$ and $z \sim 3.3$ agrees well with the $z \sim 0$ curve. The best-fit relation of the Li et al. (2023) sample is also included.

The MQN01 galaxies lie closer to the reference field galaxies on the FMR plane than to the MZR. To calculate the mean difference with field galaxy samples, we followed the MC procedure described in Sect. 4.2. Since the FMR reference from Sanders et al. (2021) is a derivative of their MZR and SFR relations and the explicit uncertainties for its combined parameters are not provided, we accounted for the model uncertainty by adopting the characteristic scatter of the constituent relations. We incorporated a mean 1σ uncertainty of 0.03 for the MZR and 0.15 for the SFR. For galaxies with $\log M_*/M_\odot > 9$, the MQN01 galaxies show a mean offset of 0.12 ± 0.12 on the FMR compared to the reference relations from Sanders et al. (2021), while the difference is weaker than what is seen on MZR and within 1σ uncertainties. Although the reduction in the mean offset from MZR to FMR is modest (~0.05), this is partially due to dilution by points already consistent with the field MZR (Sanders et al. 2021). The FMR shows a more notable corrective effect for the remaining points. While our data at the low-mass end ($\log M_*/M_\odot < 9$, and thus lower μ_α) are limited, they remain broadly compatible with the trend of the field sample (Li et al. 2023). The better consistency between protocluster galaxies and field galaxies on the FMR than MZR suggests that the environmental effect may not sufficiently affect the fundamental regulation between star formation and metal enrichment, which is generally attributed to the complex balance between gas inflows, outflows, and feedback (Lilly et al. 2013). These interpretations still need further investigation because the FMR is sensitive to systematic uncertainties, including the choice of α, calculation of SFR, and metallicity calibrations (see also the discussions in Korhonen Cuestas et al. 2025). We therefore keep the interpretation open until further observations with consistent calibrations are available.

5.3. Sample bias and model uncertainties

Even though MQN01 exhibits a statistical metal enhancement compared to the field galaxies, the limited sample size (nine galaxies) prevents us from drawing firm conclusions with high significance. The MZR for MQN01 was derived from fitting individual scattered points, while the reference relations were based on stacked spectra. We note that when comparing with distributions of scatter points instead of stacked values, the MQN01 galaxies show no clear excess in metallicities relative to the most metal-rich field galaxies. Caution needs to be taken concerning whether the relations are biased by a few galaxies or reflect the real systematic differences.

Furthermore, differences in the sample selection criteria may introduce additional biases. For example, the sample from Li et al. (2023) was selected based on strong OIII emission, which may tend to favor galaxies with particular ionization conditions given the nonmonotonic dependence of O3 on metallicities. Galaxies with extremely low or high metallicities may be missed. In addition, high-metallicity galaxies may be more dust obscured and have weaker emission lines. Methodological differences in fitting and stacking may also introduce systematic uncertainties.

The MZR and FMR are sensitive to measurement uncertainties. The stellar mass measurements are obtained from the SED fitting. The choice of the star formation history model can introduce additional systematic uncertainties. While our fiducial delayed-τ model provides a reasonable baseline, assuming a constant SFH–as often adopted for reference field samples–could yield systematically higher stellar mass estimates. Consequently, the exact magnitude of the metallicity enhancement at the high-mass end remains sensitive to these model choices, and differences in photometric coverage between samples can also affect the constraints. Furthermore, the SFRs are estimated with different tracers. As Hα observations are not always available at $z > 3$, the SFR estimates from Sanders et al. (2020) and Li et al. (2023) are from Hβ emissions and $E(B-V)$ from SED fitting, which add uncertainties and possible systematic differences. Finally, different choices of metallicity calibrations and adopted diagnostics add further uncertainties. As shown in Fig. 8, even though we adopted the same calibration methods (Bian et al. 2018), the MZR at low mass may be highly dependent on which strong-line diagnostics are used. Larger samples with homogeneous photometry, consistent SFR tracers, and

Table 2. Best-fit mass-metallicity relation parameters for the MQN01 sample and the reference samples.

Sample	Range of $\log M_*/M_\odot$	k	$\log M_0$	Z_0	$\log M_{\rm ref}$	Z at $\log M_{\rm ref}$
MQN01	(7.5, 10.5)	0.32 ± 0.08	9.45	8.52 ± 0.06	10	8.67 ± 0.07
	(9.0, 10.5)	0.45 ± 0.15	9.49	8.46 ± 0.09	10	8.67 ± 0.12
	(7.5, 10.0)	0.15 ± 0.16	9.40	8.36 ± 0.14	8	8.15 ± 0.27
Sanders et al. (2021)	(9.0, 11.0)	0.29 ± 0.02	10	8.41 ± 0.03	10	8.41 ± 0.03
Li et al. (2023)	(6.5, 10.0)	0.16 ± 0.03	8	8.08 ± 0.03	8	8.08 ± 0.03

Notes. The pivot mass ($\log M_0$) for the MQN01 sample is the mean mass weighted by the inverse variance of the metallicities, where asymmetric errors were symmetrized by averaging the upper and lower values. The metallicities of the MQN01 sample at the pivot masses of the reference samples are also listed for comparison. We set $10^{10}\,M_\odot$ and $10^8\,M_\odot$ as the reference stellar masses ($M_{\rm ref}$) for the high- and low-mass regimes, respectively, matching the M_0 in the parameterized MZR fits of the field galaxy samples, for a direct comparison.

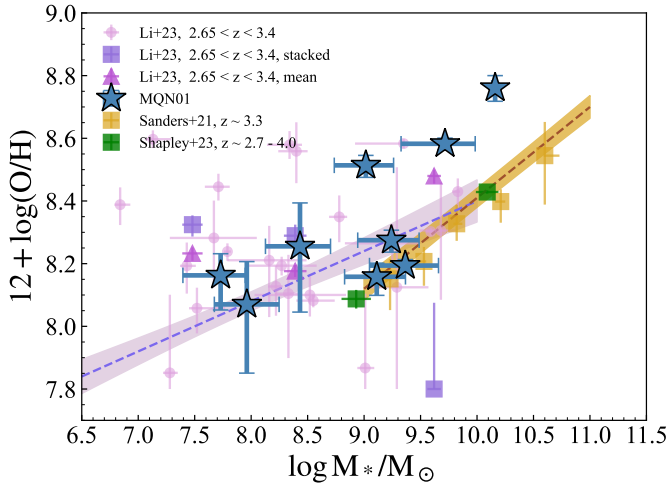

Fig. 8. Same as Fig. 6, but the metallicity for the reference datasets was calculated in the same way as for the MQN01 sample. For the CEERS sample (Green squares, Shapley et al. 2023a), the metallicities were calculated using N2, O3, and O3N2 with Bian et al. (2018) calibrations, while for the samples in Li et al. (2023, purple circles and squares) and Sanders et al. (2021, brown squares), the metallicities were calculated using O3 alone.

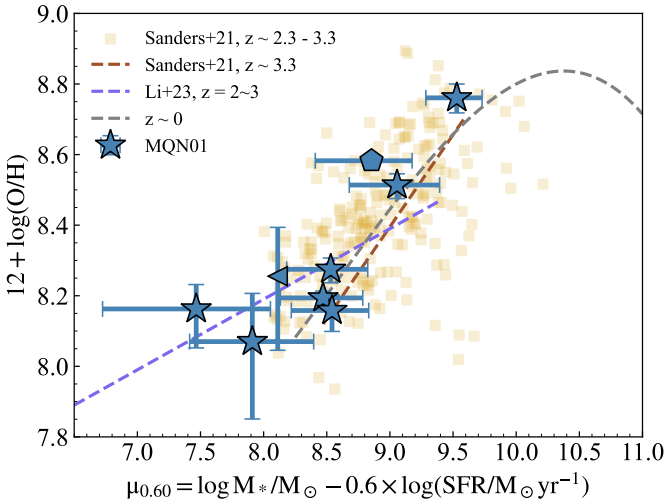

Fig. 9. Gas-phase metallicity vs. μ_α, known as the fundamental metallicity relation. The x-axis $\mu_\alpha = \log M_*/M_\odot - \alpha \log(\mathrm{SFR}[\mathrm{M}_\odot\,\mathrm{yr}^{-1}])$. We adopt the value of $\alpha = 0.60$ from Sanders et al. (2021). Individual galaxies of the MOSDEF sample at $z \sim 2.3$ and $z \sim 3.3$ are shown as brown squares (extracted using WebPlotDigitizer). The FMR calculated by the best-fit MZR and best-fit SFMS from Sanders et al. (2021) is shown as the dashed brown line. The dashed gray line shows the best-fit cubic function to the stacks of $z \sim 0$ datasets, as presented in Eq. (10) in Sanders et al. (2021). The dashed purple line shows the best-fit relation of Li et al. (2023). The MQN01 sample is shown as blue stars. For the galaxy without an Hβ detection (ID: 6005), the SFR without dust correction is adopted and is shown as the blue triangle at the upper limit of $\mu_{0.60}$. The galaxy without JWST photometry is marked as a pentagon.

uniform metallicity calibrations, as well as constraints on the detailed SFHs, will be essential to establish a more complete description of environmental effects on the MZR and FMR at $z \sim 3$.

6. Conclusions

We presented the mass-metallicity relation for a sample of nine star-forming galaxies in the MUSE Quasar Nebula 01 (MQN01) field, a massive cosmic web node at $z \sim 3.245$, containing one of the highest overdensities of galaxies and AGNs known at these redshifts. Compared with field galaxies at similar redshifts, the MQN01 sample shows a metallicity enhancement of $\sim$0.26 dex on average on the mass-metallicity relation with similar slopes. The enhancement is more prominent at higher stellar mass ($\log M_*/M_\odot > 9$) and is less significant at lower stellar mass. The differences between MQN01 and field galaxies are less significant on the fundamental metallicity relation, where the metallicity is a function of $\mu_{0.60} = \log M_* - 0.6 \log \mathrm{SFR}$. The enhanced metallicities of MQN01 suggest that galaxies in dense environments may experience more efficient or earlier stellar mass growth and metal enrichment than their field counterparts. These results provide one of the first views of mass-metallicity relations in protoclusters at $z \sim 3$, especially for one of the most overdense environments at $z \gtrsim 3$. Future observations across larger samples and broader redshift ranges will be important to test whether the features seen in MQN01 are representative of protocluster environments in the early universe, and to further understand cosmic evolution of protoclusters and relevant physical processes.

Acknowledgements. This work is supported by the European Research Council (ERC) Consolidator Grant 864361 (CosmicWeb) and by Fondazione Cariplo grant no. 2020-0902. XW acknowledges further support by Westlake University and the National Science Foundation of China (Grant No. 11821303 to SM). This work is based on observations made with the NASA/ESA/CSA *James Webb* Space Telescope. The data were obtained from the Mikulski Archive for Space Telescopes at the Space Telescope Science Institute, which is operated by the Association of Universities for Research in Astronomy, Inc., under NASA contract NAS 5-03127 for JWST. These observations are associated with program

#1835. Support for program #1835 was provided by NASA through a grant from the Space Telescope Science Institute, which is operated by the Association of Universities for Research in Astronomy, Inc., under NASA contract NAS 5-03127. This research is based on observations made with the NASA/ESA *Hubble* Space Telescope obtained from the Space Telescope Science Institute, which is operated by the Association of Universities for 15 Research in Astronomy, Inc., under NASA contract NAS 5–26555. These observations are associated with program 17065. This work is also based on observations collected at the European Southern Observatory under ESO programme (110.23ZX).

References

Adachi, K., Kodama, T., Pérez-Martínez, J. M., Suzuki, T. L., & Onodera, M. 2025, ApJ, 994, 4
Andrews, B. H., & Martini, P. 2013, ApJ, 765, 140
Astropy Collaboration (Price-Whelan, A. M., et al.) 2022, ApJ, 935, 167
Baldry, I. K., Balogh, M. L., Bower, R. G., et al. 2006, MNRAS, 373, 469
Baldwin, J. A., Phillips, M. M., & Terlevich, R. 1981, PASP, 93, 5
Behroozi, P. S., Wechsler, R. H., & Conroy, C. 2013, ApJ, 770, 57
Bian, F., Kewley, L. J., & Dopita, M. A. 2018, ApJ, 859, 175
Böker, T., Beck, T. L., Birkmann, S. M., et al. 2023, PASP, 135, 038001
Boquien, M., Burgarella, D., Roehlly, Y., et al. 2019, A&A, 622, A103
Borisova, E., Cantalupo, S., Lilly, S. J., et al. 2016, ApJ, 831, 39
Bruzual, G., & Charlot, S. 2003, MNRAS, 344, 1000
Burgarella, D., Buat, V., & Iglesias-Páramo, J. 2005, MNRAS, 360, 1413
Calzetti, D., Armus, L., Bohlin, R. C., et al. 2000, ApJ, 533, 682
Cardelli, J. A., Clayton, G. C., & Mathis, J. S. 1989, ApJ, 345, 245
Casali, M., Pirard, J.-F., Kissler-Patig, M., et al. 2006, SPIE Conf. Ser., 6269, 62690W
Chabrier, G. 2003, PASP, 115, 763
Chartab, N., Mobasher, B., Darvish, B., et al. 2020, ApJ, 890, 7
Chartab, N., Mobasher, B., Shapley, A. E., et al. 2021, ApJ, 908, 120
Cleri, N. J., Olivier, G. M., Backhaus, B. E., et al. 2025, ApJ, 994, 146
Cresci, G., Mannucci, F., & Curti, M. 2019, A&A, 627, A42
Curti, M., Cresci, G., Mannucci, F., et al. 2017, MNRAS, 465, 1384
Curti, M., Mannucci, F., Cresci, G., & Maiolino, R. 2020, MNRAS, 491, 944
Curti, M., Maiolino, R., Curtis-Lake, E., et al. 2024, A&A, 684, A75
Davé, R., Finlator, K., & Oppenheimer, B. D. 2011, MNRAS, 416, 1354
Davé, R., Finlator, K., & Oppenheimer, B. D. 2012, MNRAS, 421, 98
Dekel, A., Sari, R., & Ceverino, D. 2009, ApJ, 703, 785
Du, X., Shapley, A. E., Reddy, N. A., et al. 2018, ApJ, 860, 75
Ellison, S. L., Patton, D. R., Simard, L., & McConnachie, A. W. 2008, ApJ, 672, L107
Erb, D. K., Shapley, A. E., Pettini, M., et al. 2006, ApJ, 644, 813
Ford, H. C., Bartko, F., Bely, P. Y., et al. 1998, SPIE Conf. Ser., 3356, 234
Galbiati, M., Cantalupo, S., Steidel, C., et al. 2025, A&A, 696, A95
Genzel, R., Tacconi, L. J., Lutz, D., et al. 2015, ApJ, 800, 20
Gordon, K. D., Clayton, G. C., Misselt, K. A., Landolt, A. U., & Wolff, M. J. 2003, ApJ, 594, 279
Greene, J. E., Labbe, I., Goulding, A. D., et al. 2024, ApJ, 964, 39
Groves, B. A., Heckman, T. M., & Kauffmann, G. 2006, MNRAS, 371, 1559
Guo, Y., Koo, D. C., Lu, Y., et al. 2016, ApJ, 822, 103
Hao, L., Strauss, M. A., Tremonti, C. A., et al. 2005, AJ, 129, 1783
Hao, C.-N., Kennicutt, R. C., Johnson, B. D., et al. 2011, ApJ, 741, 124
Henry, A., Rafelski, M., Sunnquist, B., et al. 2021, ApJ, 919, 143
Jakobsen, P., Ferruit, P., Alves de Oliveira, C., et al. 2022, A&A, 661, A80
Jones, T., Martin, C., & Cooper, M. C. 2015, ApJ, 813, 126
Kacprzak, G. G., Yuan, T., Nanayakkara, T., et al. 2015, ApJ, 802, L26
Kewley, L. J., Maier, C., Yabe, K., et al. 2013, ApJ, 774, L10
Kissler-Patig, M., Pirard, J. F., Casali, M., et al. 2008, A&A, 491, 941
Kocevski, D. D., Onoue, M., Inayoshi, K., et al. 2023, ApJ, 954, L4
Korhonen Cuestas, N. A., Strom, A. L., Miller, T. B., et al. 2025, ApJ, 984, 188
Koyama, Y., Kodama, T., Tadaki, K.-I., et al. 2013a, MNRAS, 428, 1551
Koyama, Y., Smail, I., Kurk, J., et al. 2013b, MNRAS, 434, 423
Kulas, K. R., McLean, I. S., Shapley, A. E., et al. 2013, ApJ, 774, 130
Langeroodi, D., Hjorth, J., Chen, W., et al. 2023, ApJ, 957, 39
Lara-López, M. A., Cepa, J., Bongiovanni, A., et al. 2010, A&A, 521, L53
Li, M., Cai, Z., Bian, F., et al. 2023, ApJ, 955, L18
Li, Z., Kakiichi, K., Christensen, L., et al. 2025, A&A, 703, A106
Lilly, S. J., Carollo, C. M., Pipino, A., Renzini, A., & Peng, Y. 2013, ApJ, 772, 119
Madau, P., & Dickinson, M. 2014, ARA&A, 52, 415
Maiolino, R., Nagao, T., Grazian, A., et al. 2008, A&A, 488, 463
Mannucci, F., Cresci, G., Maiolino, R., Marconi, A., & Gnerucci, A. 2010, MNRAS, 408, 2115
McNab, K., Balogh, M. L., van der Burg, R. F. J., et al. 2021, MNRAS, 508, 157
Nakajima, K., & Maiolino, R. 2022, MNRAS, 513, 5134
Nakajima, K., Ouchi, M., Isobe, Y., et al. 2023, ApJS, 269, 33
Noll, S., Burgarella, D., Giovannoli, E., et al. 2009, A&A, 507, 1793
Oke, J. B., & Gunn, J. E. 1983, ApJ, 266, 713
Onodera, M., Carollo, C. M., Lilly, S., et al. 2016, ApJ, 822, 42
Pallottini, A., Ferrara, A., Gallerani, S., et al. 2025, A&A, 699, A6
Peng, Y.-J., Lilly, S. J., Kovač, K., et al. 2010, ApJ, 721, 193
Pensabene, A., Cantalupo, S., Cicone, C., et al. 2024, A&A, 684, A119
Pérez-Martínez, J. M., Dannerbauer, H., Kodama, T., et al. 2023, MNRAS, 518, 1707
Pirard, J.-F., Kissler-Patig, M., Moorwood, A., et al. 2004, SPIE Conf. Ser., 5492, 1763
Planck Collaboration VI. 2020, A&A, 641, A6
Popesso, P., Concas, A., Cresci, G., et al. 2023, MNRAS, 519, 1526
Popping, G., Somerville, R. S., & Trager, S. C. 2014, MNRAS, 442, 2398
Reddy, N. A., Oesch, P. A., Bouwens, R. J., et al. 2018, ApJ, 853, 56
Richardson, C. T., Wels, J., Garofali, K., et al. 2025, ApJ, 993, 154
Rieke, M. J., Kelly, D. M., Misselt, K., et al. 2023, PASP, 135, 028001
Rigby, J., Perrin, M., McElwain, M., et al. 2023, PASP, 135, 048001
Sanders, R. L., Shapley, A. E., Kriek, M., et al. 2018, ApJ, 858, 99
Sanders, R. L., Shapley, A. E., Reddy, N. A., et al. 2020, MNRAS, 491, 1427
Sanders, R. L., Shapley, A. E., Jones, T., et al. 2021, ApJ, 914, 19
Sarkar, A., Chakraborty, P., Vogelsberger, M., et al. 2025, ApJ, 978, 136
Sattari, Z., Mobasher, B., Chartab, N., et al. 2021, ApJ, 910, 57
Shapley, A. E., Steidel, C. C., Pettini, M., & Adelberger, K. L. 2003, ApJ, 588, 65
Shapley, A. E., Reddy, N. A., Sanders, R. L., Topping, M. W., & Brammer, G. B. 2023a, ApJ, 950, L1
Shapley, A. E., Sanders, R. L., Reddy, N. A., Topping, M. W., & Brammer, G. B. 2023b, ApJ, 954, 157
Shimakawa, R., Kodama, T., Tadaki, K. I., et al. 2014, MNRAS, 441, L1
Shimakawa, R., Kodama, T., Tadaki, K.-I., et al. 2015, MNRAS, 448, 666
Siebenmorgen, R., Carraro, G., Valenti, E., et al. 2011, The Messenger, 144, 9
Somerville, R. S., & Davé, R. 2015, ARA&A, 53, 51
Speagle, J. S., Steinhardt, C. L., Capak, P. L., & Silverman, J. D. 2014, ApJS, 214, 15
Steidel, C. C., Adelberger, K. L., Shapley, A. E., et al. 2005, ApJ, 626, 44
Steidel, C. C., Erb, D. K., Shapley, A. E., et al. 2010, ApJ, 717, 289
Steidel, C. C., Rudie, G. C., Strom, A. L., et al. 2014, ApJ, 795, 165
Stephenson, H. M. O., Stott, J. P., Cullen, F., et al. 2024, MNRAS, 527, 7891
Tacconi, L. J., Genzel, R., Neri, R., et al. 2010, Nature, 463, 781
Theios, R. L., Steidel, C. C., Strom, A. L., et al. 2019, ApJ, 871, 128
Travascio, A., Cantalupo, S., Tozzi, P., et al. 2025, A&A, 694, A165
Tremonti, C. A., Heckman, T. M., Kauffmann, G., et al. 2004, ApJ, 613, 898
Troncoso, P., Maiolino, R., Sommariva, V., et al. 2014, A&A, 563, A58
Tumlinson, J., Peeples, M. S., & Werk, J. K. 2017, ARA&A, 55, 389
Übler, H., Maiolino, R., Curtis-Lake, E., et al. 2023, A&A, 677, A145
van der Burg, R. F. J., Rudnick, G., Balogh, M. L., et al. 2020, A&A, 638, A112
Wang, X., Li, Z., Cai, Z., et al. 2022, ApJ, 926, 70
Wang, W., Cantalupo, S., Pensabene, A., et al. 2025, Nat. Astron., 9, 710
Wang, W., Cantalupo, S., Galbiati, M., et al. 2026, A&A, submitted [arXiv:2601.20473]
Yates, R. M., Kauffmann, G., & Guo, Q. 2012, MNRAS, 422, 215

Appendix A: Measurements of the MQN01 sample

In this section we present a summary Table A.1 of the measured and derived properties of galaxies in the sample, including spectroscopic redshifts, stellar mass, SFR derived from Hα flux and corrected for dust attenuation and slit loss, line ratios (log[OIII]λ5008/Hβ and log [NII]λ6585/Hα), and gas-phase metallicity (12 + log(O/H)) from Bian et al. (2018) calibrations.

Appendix B: Integrated spectra and images of the MQN01 sample

In this section we show the integrated 1D spectra and composite false-color images for the MQN01 sample in Fig. B.1, complementary to those shown in Fig. 2.

Appendix C: SFMS, MZR, and FMR using alternative stellar mass and SFR estimates

In this section we reproduce the star formation main sequence (SFMS), mass-metallicity relation (MZR), and fundamental metallicity relation (FMR) with the stellar mass derived from $Z_* = 0.004$ + SMC SED fitting and SFR with a conversion factor of $10^{-41.64}$. The relations are shown in Figs. C.1 and C.2. The overall trends and our main conclusions, metal enhancement compared with field galaxies and less difference on the FMR, remain unchanged.

Table A.1. Measured properties of individual galaxies in the MQN01 sample.

Galaxy ID	z	log $M_*/M_\odot$	log SFR[$M_\odot$ yr^{-1}]	log OIII5008/Hβ	log NII6585/Hα	12 + log(O/H)
3001	3.245	$10.16^{+0.02}_{-0.03}$	$1.05^{+0.36}_{-0.31}$	$0.05^{+0.17}_{-0.17}$	$-0.24^{+0.05}_{-0.05}$	$8.76^{+0.04}_{-0.04}$
1135	3.245	$9.36^{+0.29}_{-0.32}$	$1.49^{+0.03}_{-0.03}$	$0.77^{+0.02}_{-0.02}$	$-1.23^{+0.04}_{-0.05}$	$8.19^{+0.02}_{-0.02}$
3174	3.247	$9.02^{+0.25}_{-0.28}$	$-0.07^{+0.17}_{-0.15}$	$0.48^{+0.06}_{-0.05}$	$-0.61^{+0.09}_{-0.10}$	$8.51^{+0.03}_{-0.04}$
3172	3.251	$9.24^{+0.25}_{-0.30}$	$1.18^{+0.08}_{-0.08}$	-	$-1.11^{+0.06}_{-0.08}$	$8.27^{+0.03}_{-0.04}$
3201	3.253	$9.72^{+0.27}_{-0.39}$	$1.44^{+0.10}_{-0.10}$	$0.23^{+0.04}_{-0.04}$	$-0.69^{+0.04}_{-0.04}$	$8.58^{+0.02}_{-0.02}$
6003	3.251	$9.11^{+0.25}_{-0.29}$	$0.95^{+0.06}_{-0.06}$	$0.64^{+0.02}_{-0.02}$	$-1.45^{+0.11}_{-0.15}$	$8.16^{+0.05}_{-0.06}$
1165	3.239	$7.73^{+0.22}_{-0.33}$	$0.44^{+0.68}_{-0.62}$	$0.86^{+0.09}_{-0.08}$	$-1.14^{+0.19}_{-0.30}$	$8.16^{+0.07}_{-0.11}$
1116	3.231	$7.96^{+0.29}_{-0.29}$	$0.09^{+0.35}_{-0.33}$	$0.70^{+0.08}_{-0.07}$	$-1.75^{+0.25}_{-0.42}$	$8.07^{+0.14}_{-0.22}$
6005	3.229	$8.43^{+0.27}_{-0.31}$	$> 0.53^{+0.10}_{-0.09}$	> 0.39	$-1.20^{+0.23}_{-0.38}$	$8.26^{+0.14}_{-0.21}$

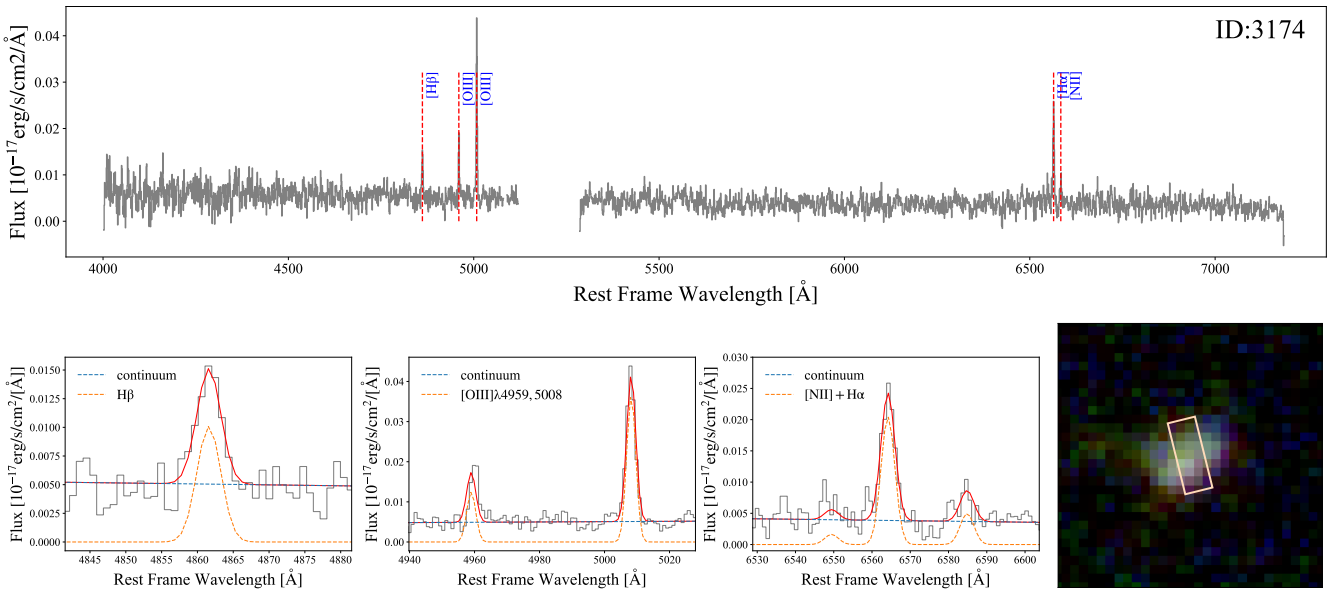

Fig. B.1. Same as Fig. 2 but for the remaining galaxies in the sample. The galaxy with ID 3201 was not observed by JWST/NIRCam and is shown in HST F814W.

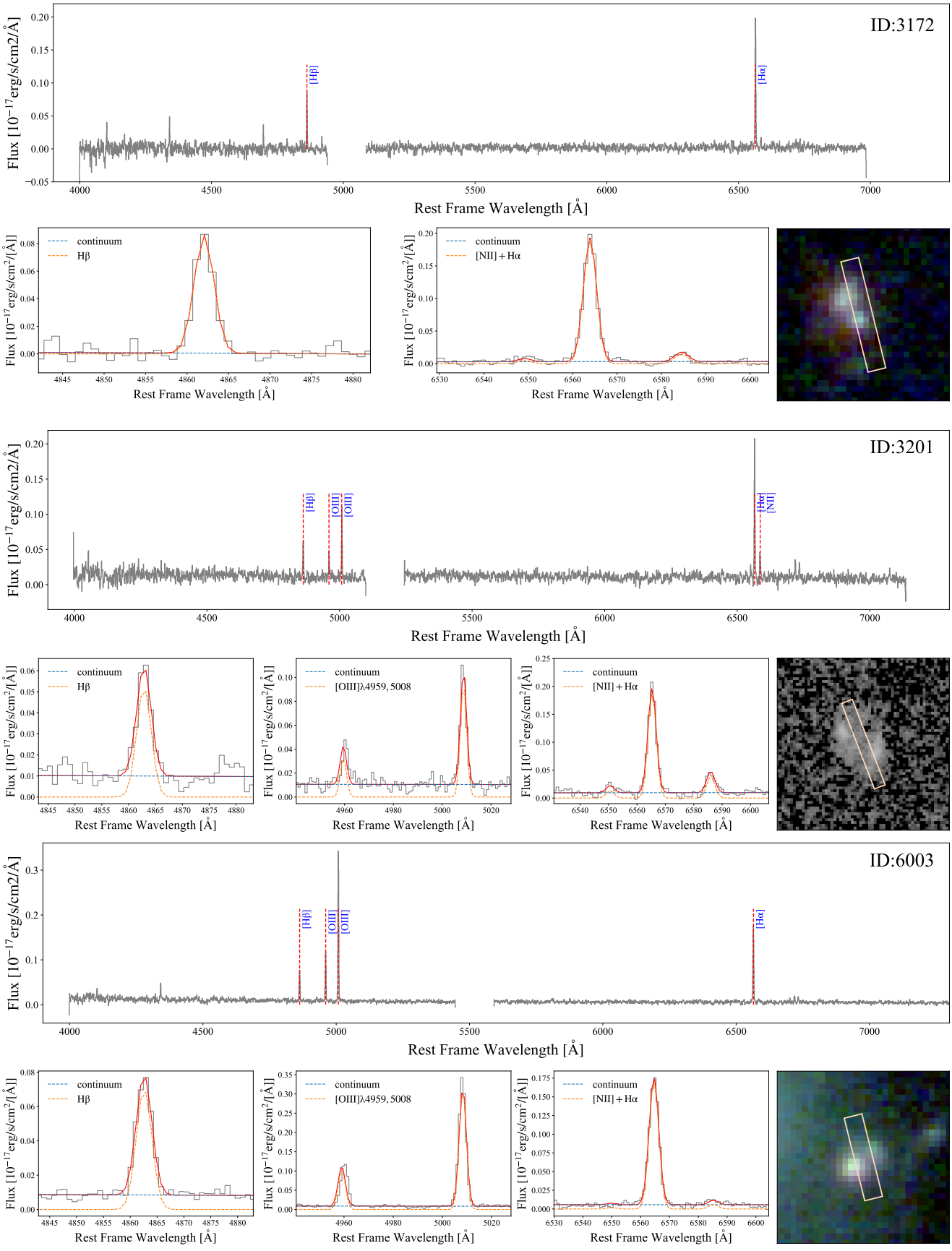

Fig. B.1. Continued.

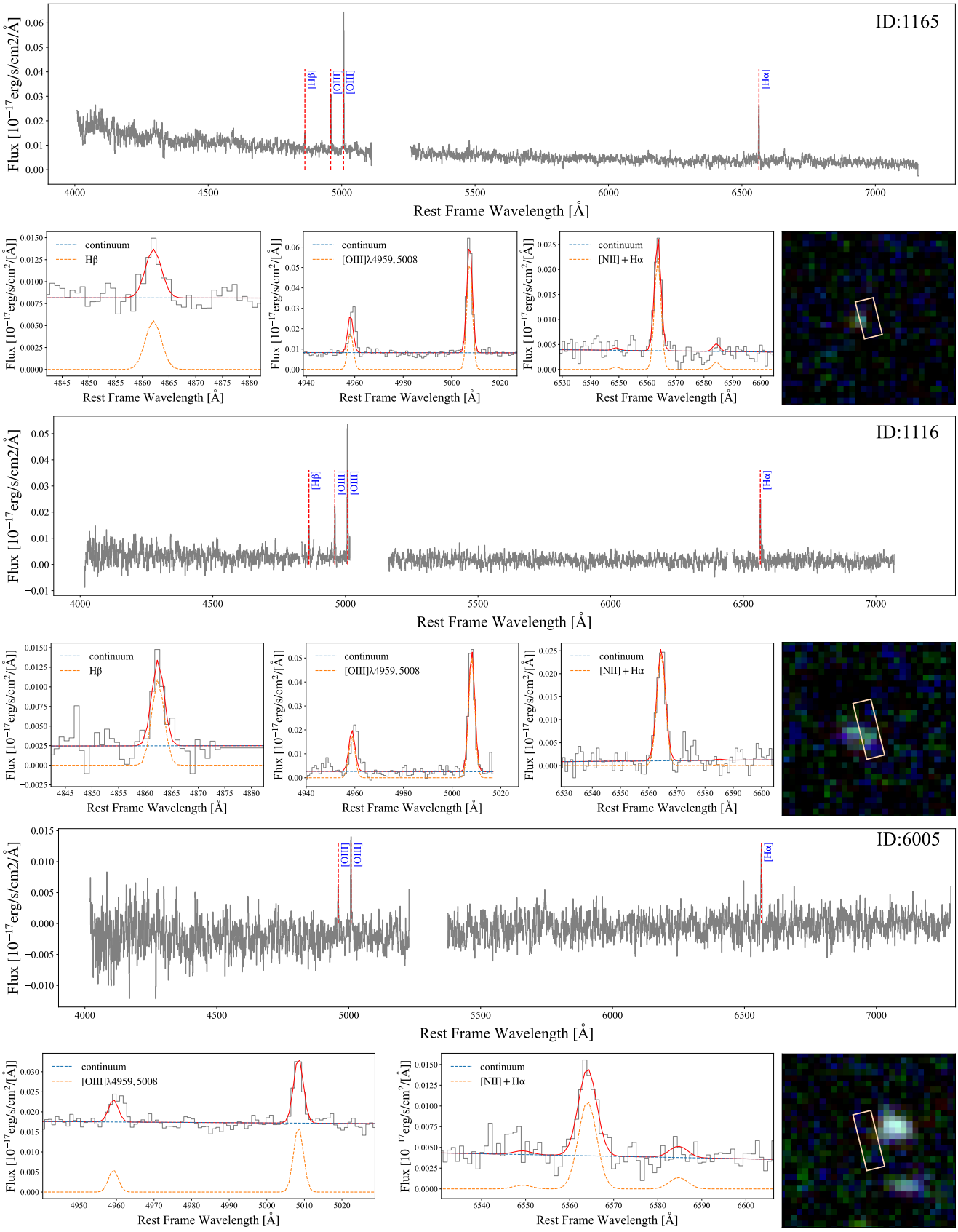

Fig. B.1. Continued.

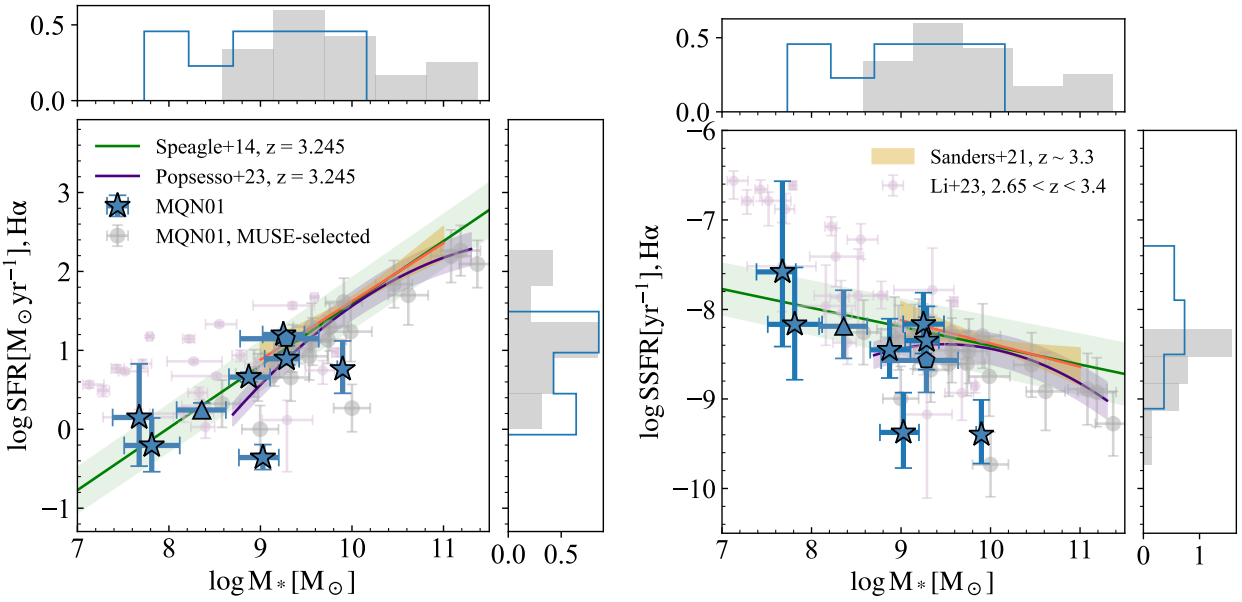

Fig. C.1. Same as Fig. 4, but the stellar mass is derived from SED fitting with $Z_* = 0.004$ and SMC extinction, and the SFR is calculated from Hα luminosity with the conversion factor of $10^{-41.64}$.

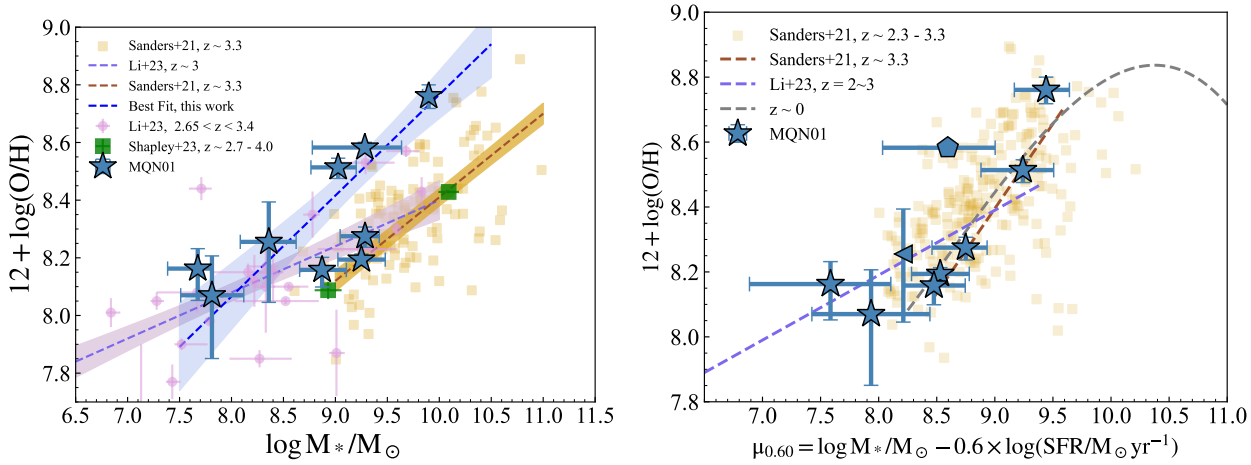

Fig. C.2. Same as Figs. 6 and 9, but the stellar mass is derived from SED fitting with $Z_* = 0.004$ and SMC extinction, and the SFR is calculated from Hα luminosity with the conversion factor of $10^{-41.64}$. The best-fit mass-metallicity relation is $12 + \log(\mathrm{O/H}) = (0.35 \pm 0.08) \times (\log(M_*/M_\odot) - 9.24) + (8.50 \pm 0.06)$.